ADVANCED FUNCTIONAL MATERIALS
www.afm-journal.de

Macroscopic Properties of Restacked, Redox-Liquid Exfoliated Graphite and Graphite Mimics Produced in Bulk Quantities

Vikram K. Srivastava, Ronald A. Quinlan, Alexander L. Agapov, John R. Dunlap, Kimberly M. Nelson, Edward Duranty, Alexei P. Sokolov, Gajanan S. Bhat, and Jimmy W. Mays**

The excellent properties exhibited by monolayer graphene have spurred the development of exfoliation techniques using bulk graphite to produce large quantities of pristine monolayer sheets. Development of simple chemistry to exfoliate and intercalate graphite and graphite mimics in large quantities is required for numerous applications. To determine the macroscopic behavior of restacked, exfoliated bulk materials, a systematic approach is presented using a simple, redox-liquid sonication process along to obtain large quantities of 2D and 3D hexagonally layered graphite, molybdenum disulfide, and boron nitride, which are subsequently characterized to observe chemical and structural changes. For MoS_2 sonicated with the antioxidant sodium bisulfite, results from Raman spectroscopy, X-ray diffraction, and electron microscopy indicate the presence of distorted phases from different polymorphs, and apparent nanotube structures in the bulk, restacked powder. Furthermore, using thermograviemtric analysis, the antioxidant enhances the resistance to oxidative degradation of MoS_2, upon thermal treatment up to 900 °C. The addition of the ionic antioxidant decreased dispersion stability in non-polar solvent, suggesting decreased compatibility with non-polar systems. Using simple chemical methods, the ability to generate tailored multidimensional layered materials with unique macroscopic properties is critical for numerous applications, including electrical devices, reinforced polymer composites, lithium–ion capacitors, and chemical sensing.

1. Introduction

The discovery of single-layer two-dimensional (2D) atomic crystals of graphene by the simple Scotch-tape exfoliation method[1] has expanded the frontier of materials research and device applications.[2] Furthermore, production of hexagonally layered heteroatomic materials known as "graphite mimics",[3,4] including transition metal dichalcogenides and boron nitride, have recently received significant attention in the scientific community.[5–7] Graphene and the corresponding mimics exhibit excellent properties, including electrical, mechanical, magnetic, thermal, sensing, and lubricating behaviors, which have broadened the scope of research for viable chemical and physical methods to tailor material properties for these applications.[2,3,7–25] Utilizing chemical functionalization (doping, intercalating, covalent grafting, etc.), numerous methods have been developed and the resulting material behaviors investigated. The synthesis

V. K. Srivastava, Dr. A. L. Agapov, K. M. Nelson, E. Duranty, Prof. A. P. Sokolov, Prof. J. W. Mays
Department of Chemistry
University of Tennessee
Knoxville, Tennessee 37996, USA
E-mail: vsrivast@utk.edu; jimmymays@utk.edu
Prof. A. P. Sokolov, Prof. J. W. Mays
Chemical Sciences Division
Oak Ridge National Laboratory
Oak Ridge, Tennessee 37831, USA
Dr. R. A. Quinlan
Materials and Power Systems Branch
Naval Surface Warfare Center Carderock Division
West Bethesda
Maryland 20817, USA
Dr. J. R. Dunlap
Department of Biochemistry and
Cellular and Molecular Biology
University of Tennessee
Knoxville, Tennessee 37996, USA
Prof. G. S. Bhat
Department of Materials Science and Engineering
University of Tennessee
Knoxville, Tennessee 37996, USA

DOI: 10.1002/adfm.201400484

of graphite intercalation compounds (GICs), first summarized in 1980, is of great interest due to the changes in material properties, especially upon restacking of the GICs.[26] By intercalating graphite with various electron donor and acceptor species, including cationic metals and halogenated reagents, chemical and structural manipulation of the graphitic sheets were observed which allowed for tuning of electrical, thermal, and magnetic properties. Recently synthesis of GICs was performed by utilizing methods such as sonication to facilitate further chemical reactions producing carbon nanoscrolls.[27] Intercalation chemistry was used to insert species between layers of IGAs such as ion intercalation of various metals in molybdenum disulfide (MoS_2)[28–30] and Lewis-acid intercalation of boron nitride (h-BN)[31] was explored to obtain restacked, layered compounds with tailored properties. Yet compared to GICs, fewer synthetic routes producing intercalated IGAs have been reported, thus bolstering the need to explore new routes.

Recently, a simple liquid exfoliation route to obtain monolayer graphene was developed to overcome the van der Waals interactions in the layered precursor,[32] and the governing parameters for exfoliation for the various liquids and graphene were explored.[33,34] The extension of this exfoliation method to MoS_2[35] and h-BN[36] powders was recently reported,[37] and both the utility and scope of this method further pursued.[24,38–40] Despite the extensive applications of sonochemistry, the addition of chemical reagents to generate new, unique materials has only just recently been explored with graphite.[41,42] However only small quantities were generated and both processes required non-ideal reaction conditions (high solvent toxicity, exfoliation pre-treatment, intense sonication conditions, difficulty in reagent/solvent removal, etc.), thus requiring improvement of this exfoliation technique for scaling up the process and achieving changes in macroscopic properties. As size-selection was not performed, the sonochemical liquid fragmentation process employed to produce 2D and 3D layered restacked powders can be understood by **Scheme 1**.

In this work, we present a facile, redox-liquid exfoliation method, which produces high-yields of various 2D and 3D structures in the absence of and using various antioxidants by mild sonication of precursor powders of graphite, molybdenum disulfide, and boron nitride in isopropanol (IPA). Dried, restacked powders of liquid and redox-liquid exfoliated samples (Table S1, Supporting Information) were characterized to determine chemical and structural characteristics. To minimize errors in measurements, which were shown to greatly depend on sample preparation and handling,[38] homogenization of the samples after sonication was performed. Investigating the effects of chemical and structural compositions of bulk quantities to observe macroscopic behavior could further broaden the utility of these materials for further chemistry and applications.

2. Results and Discussion

We prepared the 2D and 3D layered materials in high-yields using a simple sonication liquid- and redox-liquid exfoliation procedure. Ultrasonication can greatly increase sample oxidation,[43] which was initially observed for graphene isolated from graphite,[32] antioxidants were used to minimize this affect. Previously the addition of antioxidant and a radical scavenger to pretreated exfoliated graphene generated, upon isolation, MWNTs[41] and large, pristine graphite sheets.[42] However, due to low yields the properties of these structures were not investigated further. As changing the dimensionality and scaling of these materials can greatly affect their respective electronic, mechanical, and lubricating properties,[2] we analyzed the thermal, chemical, structural, and electrical behavior of the bulk fragmented samples consisting of 2D and 3D layered materials.

Previously, large quantities of intercalated and exfoliated 2D MoS_2 were produced using sodium napthalenide,[44] however this method required the use of hydrazine hydrate as a preliminary reduction treatment. Using a method to attempt to simplify the reduction and intercalation process of MoS_2, redox-liquid exfoliation of the powder was performed. As surface and edge chemistry can be greatly affected by the sonochemical process, the fragmented, restacked products were analyzed by X-ray photoelectron spectroscopy (XPS) to determine surface functionalities. Results from XPS measurements of the restacked MoS_2 products (**Figure 1**) display signature peaks for Mo^{4+} assigned to the 2H-MoS_2 structure.

Atomic percentages from multiplex measurements attributed to surface compositions were also determined (Table S2, Supporting Information). The peaks of the $Mo3d_{5/2}$ and $Mo3d_{3/2}$ were seen at ≈229.8 and ≈233.0 eV, respectively, for all samples, slightly upshifted from reported results.[45] The characteristic $S2p_{3/2}$ and $S2p_{1/2}$ peaks also can be seen for each sample at ≈162.6 and ≈163.8 eV, respectively. The apparent lack

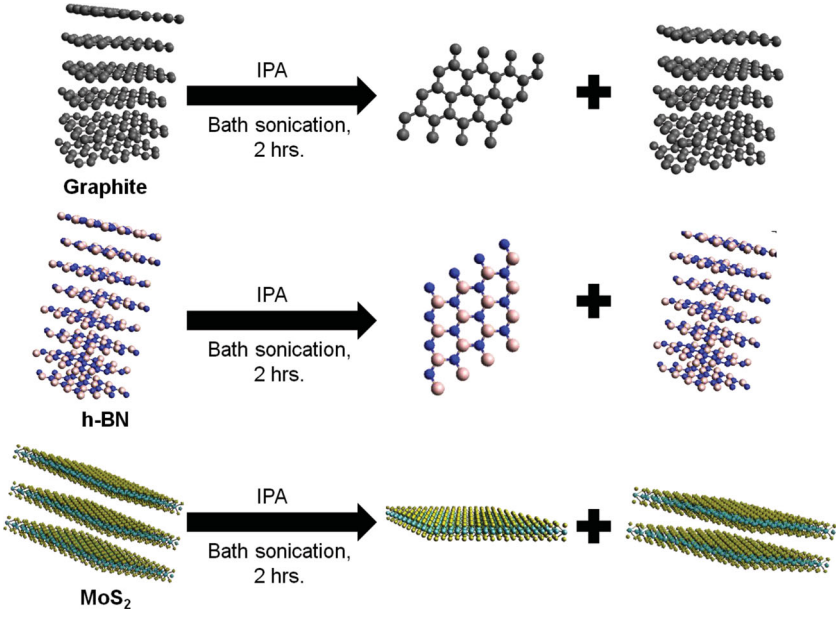

Scheme 1. Proposed schematic of sonochemically produced 2D and 3D layered compounds in bulk samples.

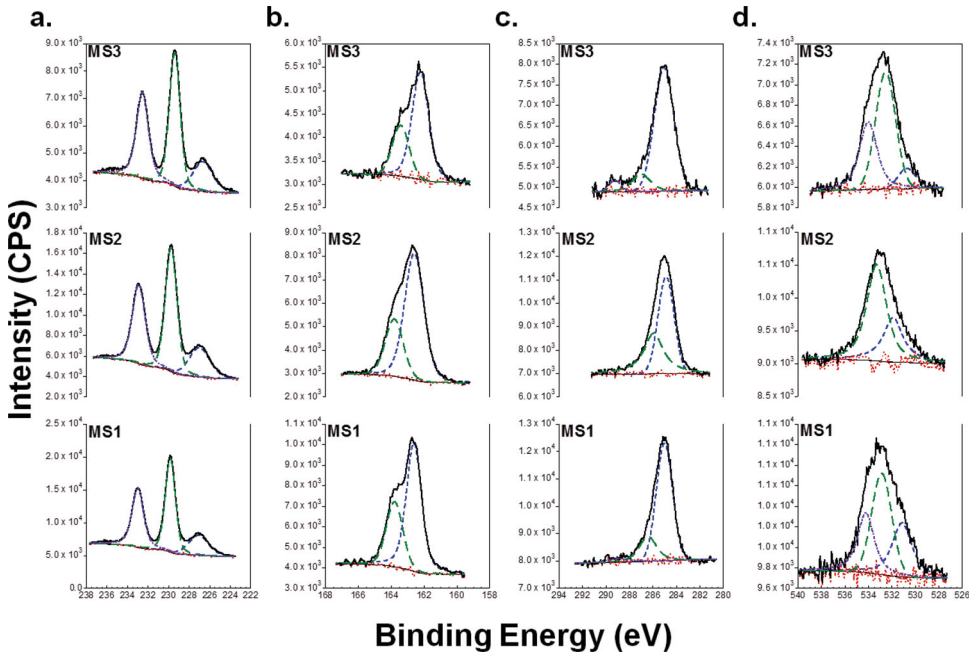

Figure 1. XPS plots of a) Mo3d, b) S2p, c) C1s, and d) O1s signature peaks of the fragmented MoS_2 samples.

of 1T-MoS_2 species in each sample were observed, in agreement with previously reported results.[46] The S2p peak at ≈167 eV corresponding to SO_3^{2-} and SO_4^{2-} ions was not seen for sample MS2, confirming no residual bisulfite. Measurements of C1s and O1s spectra indicated the presence of organic moieties in the exfoliated MoS_2 products. MS1 exhibited three C1s sub-peaks at ≈285.0, ≈286.3, and ≈289.1 eV which represent likely adventitious carbon, C-OH or C-O-C, and C(=O)OH or O-C-O functionalities, respectively. The O1s spectra contained a sub-peak at ≈531.3 eV which could be from C=O functionality or possibly the presence of MoO_2 which has previously demonstrated an O1s sub-peak at 530.7eV.[47] For samples MS2, the C1s peaks indicate the possible presence of a surface film composed primarily of carbon species. However, the O1s peak was found to contain two sub-peaks at ≈531.9 and ≈533.5 eV attributed to various C–O species. Expectedly, sample MS3 exhibited C1s peaks (≈285.0, ≈286.5, and ≈289.2 eV) and O1s peaks (≈531.6 and ≈533.3 eV) at the similar peak values seen for MS2. Qualitatively comparing the differences between the peak values of MS2 and MS3, the changes likely arise from lower concentration of oxidized carbon species in MS3.

The ATR-FTIR spectrum of precursor MoS_2 (Figure S3b, Supporting Information) powder is similar to that of dried MoS_2.[48] After sonication, the exfoliated sample MS1 displays similar peaks, slightly more intense than those of the precursor powder. A new peak of broad intensity is observed at 1732 cm^{-1} representing –C=O stretching expected from oxidation of isopropanol to acetone during pyrolysis.[49] The broad peak at 941 cm^{-1} corresponds to terminal –Mo=O bonding[50] due to potential oxidation. This is further supported by the sharply intense peaks at 730 cm^{-1} and 717 cm^{-1} characteristic of –Mo-O vibrations.[51] A similar spectrum was observed for sample MS3 indicating the presence of –Mo=O and –Mo–O bonding. For MS2, new peaks are seen at ≈2949 cm^{-1}, ≈2867 cm^{-1}, ≈1376 cm^{-1}, ≈997 cm^{-1}, and ≈973 cm^{-1}, and the peaks previously assigned to surface oxidation are not observed. The –C–O stretching peak appears at ~1166 cm^{-1} and is more easily observed compared to samples MS1 and MS3. The peaks at ≈2949 cm^{-1} and ≈2867 cm^{-1} indicate new –C–H stretches, and the sharp peak at 1457 cm^{-1} indicates a single $–CH_3$ stretch. The high intensity peak at ≈1376 cm^{-1} likely is from sulfonic/sulfate species generated from thermal degradation of sodium bisulfite.

Raman spectroscopy was performed on the samples to determine structural changes and the number of layers of the aggregates (**Figure 2**a). Noticeably, precursor MoS_2 exhibited A_{1g} and E^1_{2g} modes (corresponding full-width at half maximum (FWHM) values are given in parentheses) of 406 cm^{-1} (5.2 cm^{-1}) and 381 cm^{-1} (5.3 cm^{-1}) respectively, corresponding to the wavenumbers seen previously in bulk crystalline MoS_2.[52] Phonon confinement from small sheet sizes or defects in structure could account for precursors displaying various values for the A_{1g} and E^1_{2g} modes and their respective peak broadenings.[53] After exfoliation, both modes were observed to have shifted downfield, and the corresponding FWHM values changed as well. For sample MS1, the A_{1g} and E^1_{2g} modes were seen at 403 cm^{-1} (6.2 cm^{-1}) and 377 cm^{-1} (5.0 cm^{-1}), suggesting a decrease in layers (based on the increase in the FWHM value of the A_{1g} mode), previously observed for sonication-assisted exfoliated samples.[37] Raman analysis of sample MS2 exhibited A_{1g} and E^1_{2g} modes at 404 cm^{-1} (6.6 cm^{-1}) and 378 cm^{-1} (5.8 cm^{-1}) respectively, while sample MS3 showed A_{1g} and E^1_{2g} modes at 404 cm^{-1} (6.2 cm^{-1}) and 377 cm^{-1} (5.4 cm^{-1}), respectively. Sample MS2, displayed a peak of significant intensity at 283 cm^{-1}, characteristic of the E_{1g} mode of MoS_2 which is considered forbidden in Raman backscattering if the sample surface is perpendicular to the c-axis.[53] Considering that this peak only arises if the laser light is p-polarized,[54] we believe the observed E_{1g} mode results from the incident light scattering parallel to

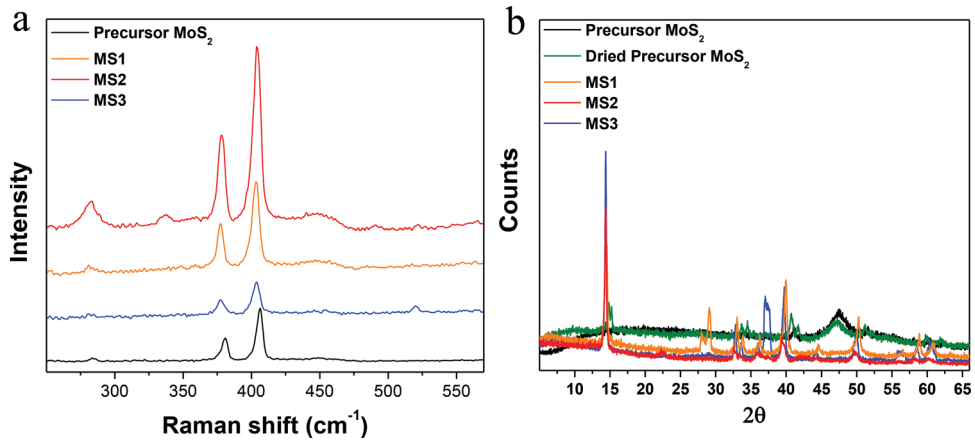

Figure 2. Obtained plots from a) Raman spectroscopy and b) XRD analysis of the fragmented MoS_2 powders.

edges of sheets or c-axis oriented sheets. Also observed in the Raman spectra of MS2 was a broad peak at ≈330 cm^{-1} previously reported for exfoliated monolayer MoS_2.[55] This corresponds to the Raman active J_3 peak in 1T-MoS_2 (not observed in 2H-MoS_2) which was present in the Raman spectrum of exfoliated lithium intercalated MoS_2 sheets.[45] The appearance of this peak suggested that sodium ions are intercalated between the MoS_2 layers forming the 1T-MoS_2 structure.

The powder X-ray diffraction (XRD) pattern of MoS_2 has been known to display various peaks based on sample purity, structure, processing (heating), exposure to air, and other factors.[56–59] However, a peak of high intensity should be visible, assigned to the (002) peak of 2H-MoS_2.[59] The (002) Bragg peak should be observed in bulk MoS_2 at $2\theta \approx 14.8°$, which can be used to determine d-spacing along the c-axis. Interestingly, the obtained XRD patterns of the MoS_2 samples (Figure 2b) indicate significant differences in this characteristic peak. Due to the precursor exhibiting no (002) peak, it was vacuum-dried at 200 °C for 14 hours but still did not display the characteristic (002) peak. The presence of sample impurities and structural heterogeneity of the precursor could account for the observed for the lack of the (002) peak and suggests highly disordered or amorphous material. However for both the precursor and dried precursor, broad peaks centered at $2\theta \approx 47°$ were observed likely due to trapped water between layers.[59] The characteristic (002) peak was observed for sample MS1 at $2\theta \approx 14.52°$, corresponding to a d-spacing along the c-axis of ≈0.609 nm, slightly less than the spacing of pristine MoS_2.[45] This decrease could arise from removal of impurities and trapped water after exfoliation. Samples MS2 and MS3 displayed (002) peaks at $2\theta = 14.36°$ and $2\theta = 14.39°$, respectively. From these peaks, the d-spacings calculated for MS2 and MS3 were ≈0.616 nm and ≈0.615 nm respectively, indicative of increased interlayer distance. The FWHM values for the (002) peaks of MS1, MS2, and MS3 were found to be 0.38°, 0.24°, and 0.20° respectively (±0.01°). We assume the lower FWHM values for MS2 and MS3 (in comparison to MS1) arise from either distortions from the presence of MoS_2 polymorphs or increased crystallite size.[56] MS1 displays a broad peak (doublet) at $2\theta \approx 28°–29°$, possibly from water[59] or from molybdenum oxides.[47] Interestingly a peak at $2\theta \approx 36.2°$ (d-spacing = 0.248 nm) is also present which could be from the hydroxylated MoO_xH_y phase[47] and/or the presence of molybdenum (IV) dioxide (MoO_2).[60,61] Also visible in the XRD pattern are the (100), (103), (105), and (110) peaks and various other 2H-MoS_2 reflections.[62] The presence and intensity of these peaks are distinguishable from those observed for the 3R-MoS_2 structure,[57] which are observed in the XRD patterns. Sample MS1 displays the (100), (103), (105), and (110) peaks of the 2H-MoS_2 structure of much higher intensity compared to samples MS2 and MS3. Previously this has been characteristic of better rotational ordering,[59] but structural variation would also affect signal intensities. Furthermore MS2 displays the lowest peak intensities and corresponding FWHM values were assigned to the 2H-MoS_2 structure, which potentially could result from sample heterogeneity due to the presence of the rhombohedral (3R-MoS_2) polymorph structure. The (103) peak of the 2H-MoS_2 polymorph appears as a doublet of low intensity, which could be assigned to the (104) and (105) peaks of the 3R-MoS_2 polytype.[57] The presence of these peaks could arise from stacking disorder from inorganic fullerene (IF-MoS_2) or nanotube (INT-MoS_2) structures, but chemical intercalation of sodium ions would also distort the hexagonal structure of layered MoS_2 to form 3R-MoS_2 polymorphs.[44] Therefore the structural behavior observed by XRD must be further correlated to electron microscopy.

Further observations to changes in structure were obtained using high resolution-transmission electron microscopy (HR-TEM) micrographs and selected area diffraction (SAED) patterns of MS1, MS2, and MS3 (**Figure 3**). A caveat of TEM analysis is the consideration of knock-on damage from electron irradiation of the samples. At specific operating voltages, knock-on damage can occur, thus creating topological defects and structural distortions which has recently garnered interest as a route for engineering new materials.[63] Defects generated by knock-on damage differed significantly between samples. HR-TEM images of MS1 exhibit transparent regions and layered sheets containing numerous layers, but interestingly the SAED pattern for MS1 indicates distortions in the hexagonally structured crystallinity,[64] similar to the SAED pattern of G1 (Figure S9c, Supporting Information) and possibly resulting from amorphous material at folded edge boundaries.[65] For MS2, ripples are observed in the aggregated sheets similar to those seen in monolayer samples[65] and edges appear to contain tube-like structures as suggested from XRD. The

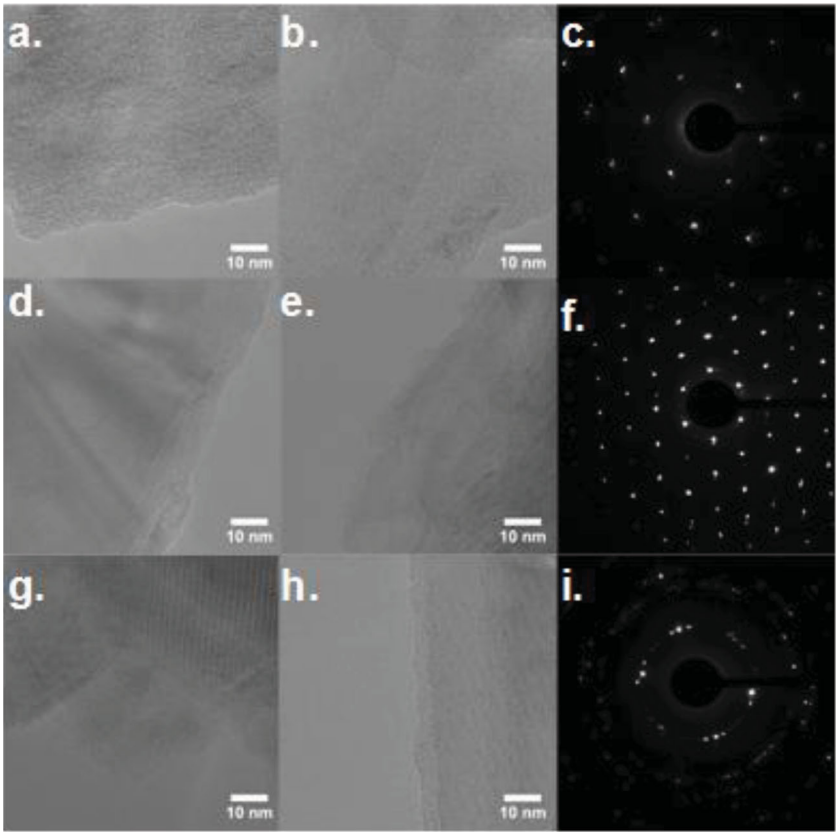

Figure 3. HR-TEM micrographs of a–b) MS1 (c: SAED pattern), d–e) MS2 (f: SAED pattern), and g–h) MS3 (i: SAED pattern).

corresponding SAED pattern displays bright intensity spots characteristic of rotationally stacked aggregates demonstrating highly ordered hexagonal crystalline domains, as seen in exfoliated few layer or monolayer MoS_2.[45,66] The HR-TEM images of MS3 display ordered crystalline layers similarly seen for G3 (Figure S9g-h, Supporting Information), however the SAED pattern displays no hexagonal symmetry of the (001) diffraction spots but displays high intensity (110) spots indicative significant stacking faults along the edges of the layered sheets.[64] The corresponding SAED patterns clearly display the differences in the stacking order of sheet aggregates.

Scanning electron microscopy (SEM) images of the exfoliated MoS_2 products (**Figure 4**) display large-scale variations in sheet size and structure. The images were obtained from solutions of dispersed exfoliated MoS_2 products of similar concentrations drop cast onto carbon grids.

Fragmented sheets containing numerous layers are visible, all of which display lateral lengths ($\langle l \rangle$) of $\langle l \rangle \leq 2$ µm. A majority (~85%) appeared to have lateral lengths corresponding to $\langle l \rangle \leq 1.5$ µm, indicative of the edge fragmentation process accounting for any nanoscale sheets. Each sample contains nanometer length fragments on the surfaces, although much smaller fragments are seen in sample MS2. Images of samples MS2 and MS3 exhibited less amorphous and more highly defined sheets as compared to those of sample MS1. The image of MS2 (Figure 4c) contains a multilayered sheet with folded layers and highly defined sheet edges. Overall, between samples, no major difference was observed for the number of layers of each crystalline sheet, but edge characteristics do appear to differ between the samples.

Thermal properties of the precursor and exfoliated products were measured to observe any absorbed organic moieties and changes in thermal resistance to oxidation. The measured temperature at maximum weight loss, T_{max}, and residual weight percentages were obtained from the TGA curves (Table S3, Supporting Information). For the control sample MS1, two minor thermal degradations (T_{min1} and T_{min2}) were observed at 475 °C and 382 °C, respectively, likely a result of thermal oxidation. The TGA plot of MoS_2 exfoliated in the presence of sodium bisulfite, referred to as sample MS2, displayed enhanced thermal resistance to oxidation as initial oxidative degradation occurred at T_{min1} and T_{min2} values of 496 °C and 395 °C respectively. The MoS_2 powder retained 3.0 wt.% upon oxidative degradation, but samples MS1, MS2, and MS3 retained residual weights of 15.2 wt.%, 54.0 wt.%, and 17.8 wt.% respectively, demonstrating decreased susceptibility to thermal oxidation. Comparatively, sample MS2 displayed significantly better resistance to thermal oxidation compared to the other samples.

TGA coupled with mass spectrometry (TGA-MS) measurements were performed in inert conditions (N_2) of the precursors along with corresponding ion (mass/charge) currents to observe evolved CO_2 ($m/z = 44$) during the heating process from absorbed organic residues. Ultra-high purity N_2 gas was used to minimize the presence of absorbed or trapped O_2 gas to prevent oxidative combustion. TGA-MS plots (Figure S11b, Supporting Information) of the exfoliated MoS_2 samples demonstrate the differences in thermal behavior. Ion current values and normalized ion current ratios were tabulated for comparison (Table S4, Supporting Information). Precursor MoS_2 displayed a weight loss of 4.4 wt.%, indicative of some residual impurities in the material. This may be caused by absorbed hydrocarbon/gaseous species or from oxidized edges or surface chemistry. Sample MS1 displays a loss of 5.3 wt.%, indicating retention of little organic/water residue, however much less than absorbed surfactant retained on exfoliated MoS_2 nanosheets.[66] This is further supported by the value for the normalized ratio of ion current signals between both samples, (0.96), indicating that both samples produced roughly the same concentration of evolved CO_2 gas. Contrastingly, samples MS2 and MS3 exhibited significant losses of 26.2 wt.% and 21.9 wt.%, respectively. Interestingly, observing the evolved CO_2 gas signal ratios, substantially higher levels of evolved CO_2 were observed for both samples as compared to the precursor and sample MS1. While increased trapped CO_2 gas may contribute to these increases, the significant formation of CO_2 gas occurs in the temperature range of 700–900 °C. This increase could be from

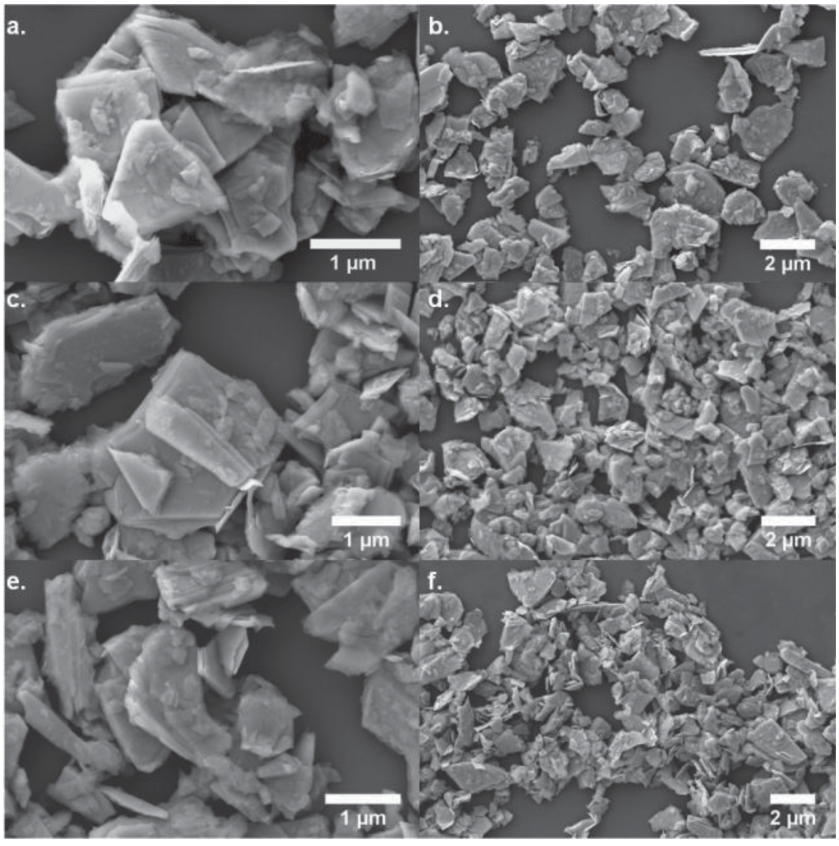

Figure 4. SEM images of exfoliated MoS_2 products: a–b) MS1, c–d) MS2, and e–f) MS3.

trapped gas or small organic molecules, but likely reflect the presence of a large oxygen containing species such as polymer. Significantly, for sample MS2, the released CO_2 gas increased by nearly 5 times compared to precursor MoS_2. As nanoscale MoS_2 has been shown to photo-oxidize alcohols,[67] introduction of sodium bisulfite could possibly induce the polymerization of the gaseous, oxidized isopropanol, as sodium bisulfite is a redox initiator.[68] The "trapped" organic residue demonstrated excellent thermal resistance from enhanced interactions with the MoS_2 sheets.

The dispersion characteristics of materials provide critical information regarding favorable solvating conditions and particle/liquid interactions. As absorbance can be influenced by sample heterogeneity and scattering effects from the samples, the associated errors from the measurements were determined for the dispersions. Optical absorbance (UV-Vis) measurements (**Figure 5**a) of solutions were performed at various concentrations. The molar absorptivity coefficient, $\alpha\lambda$, was calculated using Beer–Lambert's law for diluted dispersions of samples G1, MS1, and BN1 in isopropanol (Table S5, Supporting Information). However these values should not be considered intrinsic to these materials, as variations in dispersed flake size can greatly affect the $\alpha\lambda$ values,[38] and therefore considered a qualitative value. The $\alpha\lambda$ values were determined at specific wavelengths, λ = 660 nm for G1, λ = 672 nm for MS1, and λ = 300 nm for BN1 to compare with previous reports.[37] Also molar absorptivity coefficients at 660 nm, α_{660nm} (ml (mg m)$^{-1}$), were calculated using Beer-Lambert's law for diluted dispersions of MS1 and BN1 in isopropanol. Since the precursor powder sizes are comparable (BN < MoS_2 < EG), as expected, we observed the inverse relationship regarding the molar absorptivity coefficients (α_{G1} (434) < α_{MS1} (1116) < α_{BN1} (1162)). A significant difference between the restacked MoS_2 samples is noticeable when dispersed in chloroform (Figure 5b), as sample MS2 demonstrates significantly poorer stability compared to MS1 and MS3. Considering results from other characterization methods and the corresponding Hansen solubility parameters (Table S5, Supporting Information), decreased dispersion in $CHCl_3$ of

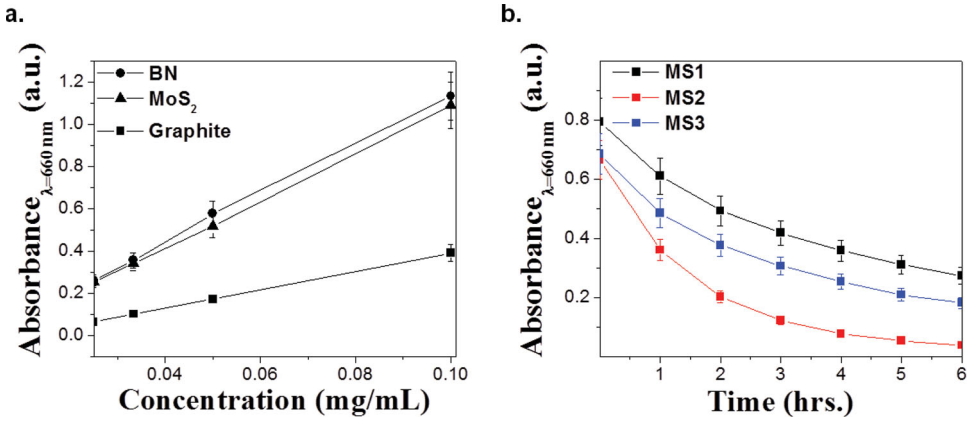

Figure 5. Optical absorbance for λ = 660 nm of a) Beer-Lambert plots for determining molar absorptivity coefficients in IPA and b) stability of exfoliated MoS_2 samples in $CHCl_3$.

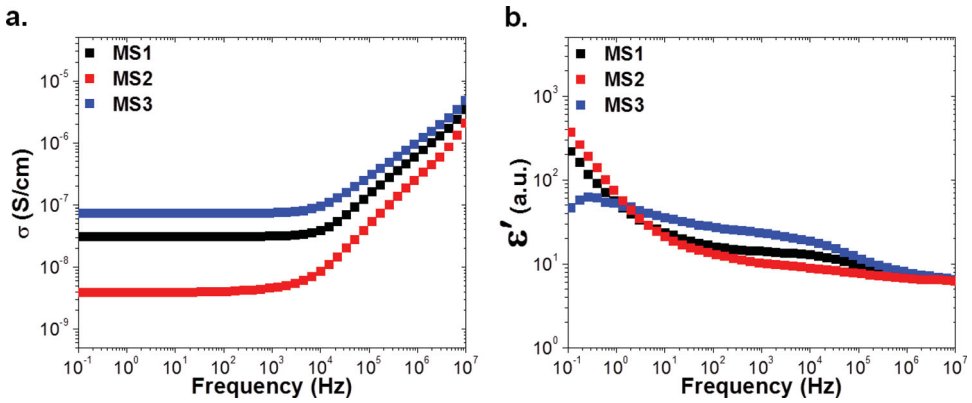

Figure 6. Dielectric measurements of a) DC conductivity, b) relative permittivity of the compacted exfoliated MoS_2 powders.

sample MS2, which appears chemically more pristine but also appears to have some physisorbed ionized organic species, is not surprising. Another possible result may be enhanced ionic characteristic due to possible intercalation of sodium ions. Thus we believe the differences in polarity between the intercalated/exfoliated samples are even observable on the macroscale, resulting from synergistic chemical differences on the exfoliated (2-D) nanoscale sheets and bulk intercalated samples.

D.C. conductivities and relative permittivities (**Figure 6**) of the macroscopic exfoliated MoS_2 samples all displayed conductivities $>10^{-9}$ S/cm. Their respective conductivities are comparable to the measured conductivity of 3.6×10^{-7} S/cm obtained from monolayer/few-layer free standing MoS_2 films.[37]

Sample MS3 exhibits the highest conductivity suggesting that the physisorbed species increased the semiconducting behavior, possibly from residual TEMPO generating a more highly polarized powder which further may be highly oxidized. MS2 comparatively appears to be insulating, with lower conductivity (≈1 order less) than both MS1 and MS3. Poor contact between layer edges from wrinkling/folding as seen by SEM (similar to sample G2), or carbon oligomer/polymer films would contribute to decreases in conductivity. This lower conductivity could result from decreased presence of oxidative edge functionality reflected by the significantly larger dielectric constant of MoO_3 compared to the constant of MoS_2.[69] The relative static permittivity (dielectric constant) of each sample was ≈6 a.u. which falls within the range of room temperature resistivity values for various MoS_2 samples.[70] The real part of the dielectric permittivity contains a step in the range of 10^4–10^5 Hz for all samples. Sample MS2 clearly has the smallest decrease in polarization whereas the biggest decrease occurs for sample MS3. We attribute this process to a Maxwell–Wagner–Sillars (MWS) polarization effect that arises due to sample heterogeneity, with a larger step usually indicating increased sample inhomogeneity.[71] As revealed by TGA-MS, XPS, and ATR-FTIR the presence of some amorphous polymeric residue in sample MS2 likely contributes to changes in the properties of the bulk powders. The weakness of MWS process for this sample probably comes from the fact that inclusions in this sample mostly consist of amorphous carbon/oxygen and hydrocarbon species (as concluded from TGA-MS, XPS, and ATR-FTIR data). This polymeric hydrocarbon and oxygen species is for the most part insulating and polar, similar to MoS_2 itself. As a result, there is not significant electric contrast between inclusions and MoS_2 sheets in sample MS2 leading to weak MWS polarization. On the other hand, the MS3 sample was exfoliated in the presence of TEMPO, which could have become intercalated between layers or physisorbed to sheet edges. This could enhance the MWS process due to increased dielectric contrast between the radical species and the exfoliated MoS_2. Various other factors could contribute to the MWS process due to the oxidation of isopropanol producing carbonyl moieties such as aldehydes, ketones, and carboxylic acids.[72] Despite enhancing dispersion in polar solvents, the presence of these physisorbed polar moieties would inhibit conductivity.

3. Conclusion

Previous work has demonstrated the difficulties to obtain monolayer nanosheets exhibiting excellent properties from larger sized 3D layered precursors. Using sonochemistry to perform redox-liquid exfoliation, we produced large quantities of graphite, molybdenum disulfide, and boron nitride consisting of 2D and 3D layered sheets and investigated the self-assembly of these materials. The addition of an ionic antioxidant, sodium bisulfite, significantly altered the chemical and structural characteristics of MoS_2. XPS and ATR-FTIR confirmed the presence of oxidized carbon species on the surface, possibly ionized polymer from sodium bisulfite acting as a reducing species coupled with sonication induced oxidation. From Raman spectroscopy and TEM images, the crystalline structure appeared to contain the 1T-MoS_2 polymorph, which would result from intercalated sodium forming Na_xMoS_2 sheets in the bulk sample. Also resistance to thermal oxidation was increased substantially for MoS_2 by simple in situ sonication with sodium bisulfite. A decrease in stability in non-polar solvent demonstrated an increase in the sedimentation of the fragmented sheets. The simple production of chemically tailored nano- and microscale materials in large quantities could be exploited to generate novel materials of desired lengths and dimensions suitable for mechanical reinforcement, high-temperature, electronic, and dielectric applications.

4. Experimental Section

Liquid-Redox Exfoliation of Bulk Precursors: The precursor powders of graphite (Sigma-Aldrich, synthetic <20 μm), h-BN (Sigma-Aldrich, <1 μm), and MoS_2 (Sigma-Aldrich, <2 μm) were used as received. The antioxidants 2,6-di-tert-butyl-4-methylphenol (Sigma-Aldrich, ≥99%), sodium bisulfite (Acros Organics, Analytical Grade), and 2,2,6,6-tetramethylpiperidine 1-oxyl (Sigma-Aldrich, 98%) and solvents 2-propanol (Fisher Scientific, Certified ACS Reagent Grade Plus ≥99.5%) and chloroform (Fisher Scientific, Certified ACS Reagent Grade ≥99.8%) were used without further purification. Solutions were made by adding of each respective precursor powder (10 mg) to glass vials containing fresh 2-propanol (10 ml). Antioxidant solutions were prepared by adding of 2,6-di-tert-butyl-4-methylphenol (1 mg) or of sodium bisulfite (10 mg), or of 2,2,6,6-tetramethylpiperidine 1-oxyl (10 mg), followed by vigorous stirring for 5 minutes prior to sonication. Subsequently, solutions were sonicated using a Fisher Scientific FS20H bath sonicator (≈70 W, 42 KHz) for 2 hours, while maintaining a constant water level and temperature ≤30 °C. Due to larger quantities required for dielectric measurements and BET analysis, solutions containing 200 mg of precursor powders were made at similar concentrations as previously described. These solutions were sonicated using a Fisher Scientific F110 bath sonicator (≈100 W, 42 KHz) for 2 hours while maintaining a constant water level and temperature ≤30 °C. After sonication, the solutions were then washed extensively with excess methanol. The solutions were then filtered using a 0.22 micron filter (PVDF), and the obtained products dried for 14 hours under vacuum. The dried powders were then collected and analyzed.

Characterization Methods: TGA was performed using a TA Instruments Q-50 TGA (±2.0 wt.%). Samples were heated from 25 °C to 900 °C in the presence of compressed air (Airgas) at a flow rate of 40 mL/min. TGA-MS measurements were performed using a TA Instruments Discovery TGA-MS (± 0.1 wt.%). Samples were dried with ultrahigh purity (UHP) N_2 (Airgas) for 15 minutes then subsequently heated from 25 °C to 900 °C in the presence of UHP N_2 (Airgas) at a flow rate of 40 mL min^{-1}. Ionization was performed using an electrospray source, and the masses of evolved gases measured from 1–300 amu using a Faraday cup detector. ATR-FTIR was carried out using a ThermoScientific Nicolet iS10 FT-IR Spectrometer equipped with a Smart iTR accessory. The XPS data were collected using a Physical Electronics model 5400 X-ray photoelectron spectrometer equipped with non-monochromatic Mg Kα (1253.6 eV) and Al Kα (1486.7 eV) X-rays. The data presented here were collected using the non-monochromatic Al Kα X-rays. The samples were mounted on the sample puck by placing a small circle of double-sided tape (<1 mm diameter) on the puck and then pressing the powder down over the puck to cover the tape. A molybdenum mask with a 3 mm diameter hole was then placed over the powder and secured with screws. The samples were placed in the introduction chamber for approximately 15 minutes and then transferred to the analysis chamber. The analysis area was set to 1.1 mm diameter spot size. During data collection, the analysis chamber pressure was approximately 1.0×10^{-9} Torr. Survey spectra were collected at low resolution, which corresponds to analyzer pass energy of 89.45 eV. They were collected in increments 0.5 eV/step and an integration interval of 50 ms/step. The complete spectrum consists of the average of 15 cycles. Multiplex spectra were collected at high resolution corresponding to analyzer pass energy of 22.35 eV with increments of 0.1 eV/step and an integration interval of 20 ms/step. Raman analysis was performed on powder samples using a JY-Horiba T64000 spectrometer using a 514 nm laser excitation (incident power ≈0.5 mW), and a CCD detector. The instrument was calibrated using microcrystalline silicon (± 0.7cm^{-1}). Wide-angle powder XRD analysis was performed on powder samples in atmospheric conditions using a Panalytical Empyrean diffractometer equipped with a Ge monochromator using Cu-Kα ($\lambda = 0.1542$ nm) radiation and a PIXcel^{3D} detector (±0.01°). Graphite and MoS_2 products were analyzed in the range of $2\theta = 5°–70°$ (step size of 0.02°), and BN products analyzed in the range of $2\theta = 15°–80°$ (step size of 0.02°). HR-TEM images were obtained using a Zeiss Libra 200 MC TEM/STEM operating at an accelerating voltage of 200 kV. SEM images were obtained using a Zeiss Auriga SEM operating at an electron accelerating voltage of 30 keV. For HR-TEM and SEM analysis, samples were prepared by casting a drop from IPA dispersions onto silicon wafers and subsequently allowing solvent to evaporate. Dielectric Spectroscopy was performed on a Novocontrol Alpha-A impedance analyzer. Powder samples were pressed similarly until compaction, and the dielectric properties (accuracy of ±5–10%) measured at room temperature with an applied external voltage of 1V. Nitrogen adsorption analysis was performed on a Micromeritics Tristar 3000 at 77 K. Prior to measurement the samples were degassed at 200 °C under flowing nitrogen overnight. For BET analysis, the specific surface area was calculated using the Brunauer–Emmett–Teller (BET) equation utilizing the adsorption branch (±0.01 $m^2 g^{-1}$). The pore size distribution plot was derived from the adsorption branch of the isotherms using the Barrett-Joyner-Halenda (BJH) method. Optical measurements were performed in the wavelength interval of 250–800 nm (±2 nm) with a Thermo Scientific Evolution 600 UV-Vis Spectrometer using Spectrosil Far UV Quartz 10 mm cuvettes (Starna Cells Inc.).

Supporting Information

Supporting Information is available from the Wiley Online Library or from the author.

Acknowledgments

This research was supported by the Office of Naval Research (Award No. N00014–10–1–0393). R.A.Q. acknowledges financial support by the Carderock Division of the Naval Surface Warfare Center's In-house Laboratory Independent Research Program administrated under ONR's Program Element 0601152N. A.L.A., K.M.N., A.P.S., and J.W.M. acknowledge partial support from the Division of Materials Science and Engineering, US Department of Energy, Office of Basic Energy Sciences.

Received: February 11, 2014
Revised: March 27, 2014
Published online: May 23, 2014

[1] K. S. Novoselov, D. Jiang, F. Schedin, T. J. Booth, V. V. Khotkevich, S. V. Morozov, A. K. Geim, *Proc. Natl. Acad. Sci. USA* **2005**, *102*, 10451.
[2] A. K. Geim, K. S. Novoselov, *Nat. Mater.* **2007**, *6*, 183.
[3] C. N. R. Rao, H. Matte, K. S. Subrahmanyam, *Acc. Chem. Res.* **2013**, *46*, 149.
[4] C. N. R. Rao, H. S. S. R. Matte, U. Maitra, *Angew. Chem. Int. Ed.* **2013**, *52*, 13162.
[5] A. K. Geim, I. V. Grigorieva, *Nature* **2013**, *499*, 419.
[6] G. H. Gao, W. Gao, E. Cannuccia, J. Taha-Tijerina, L. Balicas, A. Mathkar, T. N. Narayanan, Z. Liu, B. K. Gupta, J. Peng, Y. S. Yin, A. Rubio, P. M. Ajayan, *Nano Lett.* **2012**, *12*, 3518.
[7] M. Chhowalla, H. S. Shin, G. Eda, L. J. Li, K. P. Loh, H. Zhang, *Nat. Chem.* **2013**, *5*, 263.
[8] J. N. Coleman, *Acc. Chem. Res.* **2013**, *46*, 14.
[9] M. Quintana, E. Vazquez, M. Prato, *Acc. Chem. Res.* **2013**, *46*, 138.
[10] D. Golberg, Y. Bando, Y. Huang, T. Terao, M. Mitome, C. Tang, C. Zhi, *ACS Nano* **2010**, *4*, 2979.
[11] A. Nag, K. Raidongia, K. Hembram, R. Datta, U. V. Waghmare, C. N. R. Rao, *ACS Nano* **2010**, *4*, 1539.
[12] M. Osada, T. Sasaki, *Adv. Mater.* **2012**, *24*, 210.
[13] L. Song, Z. Liu, A. L. M. Reddy, N. T. Narayanan, J. Taha-Tijerina, J. Peng, G. H. Gao, J. Lou, R. Vajtai, P. M. Ajayan, *Adv. Mater.* **2012**, *24*, 4878.

[14] V. Georgakilas, A. B. Bourlinos, R. Zboril, T. A. Steriotis, P. Dallas, A. K. Stubos, C. Trapalis, *Chem. Commun.* **2010**, *46*, 1766.
[15] M. Xu, T. Liang, M. Shi, H. Chen, *Chem. Rev.* **2013**.
[16] X. Huang, Z. Zeng, H. Zhang, *Chem. Soc. Rev.* **2013**, *42*, 1934.
[17] C. N. R. Rao, A. Nag, *Eur. J. Inorg. Chem.* **2010**, *2010*, 4244.
[18] I. M. Allam, *J. Mater. Sci.* **1991**, *26*, 3977.
[19] S. Jeong, J. H. Han, J.-t. Jang, J.-w. Seo, J.-G. Kim, J. Cheon, *J. Am. Chem. Soc.* **2011**, *133*, 14500.
[20] A. P. M. Barboza, H. Chacham, C. K. Oliveira, T. F. D. Fernandes, E. H. M. Ferreira, B. S. Archanjo, R. J. C. Batista, A. B. de Oliveira, B. R. A. Neves, *Nano Lett.* **2012**, *12*, 2313.
[21] Y. Lin, J. W. Connell, *Nanoscale* **2012**, *4*, 6908.
[22] L. Ci, L. Song, C. H. Jin, D. Jariwala, D. X. Wu, Y. J. Li, A. Srivastava, Z. F. Wang, K. Storr, L. Balicas, F. Liu, P. M. Ajayan, *Nat. Mater.* **2010**, *9*, 430.
[23] L. Song, L. Balicas, D. J. Mowbray, R. B. Capaz, K. Storr, L. Ci, D. Jariwala, S. Kurth, S. G. Louie, A. Rubio, P. M. Ajayan, *Phys. Rev. B* **2012**, *86*.
[24] V. Nicolosi, M. Chhowalla, M. G. Kanatzidis, M. S. Strano, J. N. Coleman, *Science* **2013**, *340*, 1420.
[25] M. Quintana, A. Montellano, A. E. d. R. Castillo, G. Van Tendeloo, C. Bittencourt, M. Prato, *Chem. Commun.* **2011**, *47*, 9330.
[26] M. S. Dresselhaus, G. Dresselhaus, *Adv. Phys.* **1981**, *30*, 139.
[27] L. M. Viculis, J. J. Mack, R. B. Kaner, *Science* **2003**, *299*, 1361.
[28] G. Du, Z. Guo, S. Wang, R. Zeng, Z. Chen, H. Liu, *Chem. Commun.* **2010**, *46*, 1106.
[29] J. Heising, M. G. Kanatzidis, *J. Am. Chem. Soc.* **1999**, *121*, 11720.
[30] M. S. Whittingham, *Prog. Solid State Chem.* **1978**, *12*, 41.
[31] N. I. Kovtyukhova, Y. X. Wang, R. T. Lv, M. Terrones, V. H. Crespi, T. E. Mallouk, *J. Am. Chem. Soc.* **2013**, *135*, 8372.
[32] Y. Hernandez, V. Nicolosi, M. Lotya, F. M. Blighe, Z. Sun, S. De, I. T. McGovern, B. Holland, M. Byrne, Y. K. Gun'ko, J. J. Boland, P. Niraj, G. Duesberg, S. Krishnamurthy, R. Goodhue, J. Hutchison, V. Scardaci, A. C. Ferrari, J. N. Coleman, *Nat. Nanotechnol.* **2008**, *3*, 563.
[33] J. N. Coleman, *Adv. Funct. Mater.* **2009**, *19*, 3680.
[34] Y. Hernandez, M. Lotya, D. Rickard, S. D. Bergin, J. N. Coleman, *Langmuir* **2010**, *26*, 3208.
[35] G. L. Frey, K. J. Reynolds, R. H. Friend, H. Cohen, Y. Feldman, *J. Am. Chem. Soc.* **2003**, *125*, 5998.
[36] C. Zhi, Y. Bando, C. Tang, H. Kuwahara, D. Golberg, *Adv. Mater.* **2009**, *21*, 2889.
[37] J. N. Coleman, M. Lotya, A. O'Neill, S. D. Bergin, P. J. King, U. Khan, K. Young, A. Gaucher, S. De, R. J. Smith, I. V. Shvets, S. K. Arora, G. Stanton, H.-Y. Kim, K. Lee, G. T. Kim, G. S. Duesberg, T. Hallam, J. J. Boland, J. J. Wang, J. F. Donegan, J. C. Grunlan, G. Moriarty, A. Shmeliov, R. J. Nicholls, J. M. Perkins, E. M. Grieveson, K. Theuwissen, D. W. McComb, P. D. Nellist, V. Nicolosi, *Science* **2011**, *331*, 568.
[38] G. Cunningham, M. Lotya, C. S. Cucinotta, S. Sanvito, S. D. Bergin, R. Menzel, M. S. P. Shaffer, J. N. Coleman, *ACS Nano* **2012**, *6*, 3468.
[39] Y. Lin, T. V. Williams, J. W. Connell, *J. Phys. Chem. Lett* **2010**, *1*, 277.
[40] Y. Lin, T. V. Williams, T. B. Xu, W. Cao, H. E. Elsayed-Ali, J. W. Connell, *J. Phys. Chem. C* **2011**, *115*, 2679.
[41] M. Quintana, M. Grzelczak, K. Spyrou, M. Calvaresi, S. Bals, B. Kooi, G. Van Tendeloo, P. Rudolf, F. Zerbetto, M. Prato, *J. Am. Chem. Soc.* **2012**, *134*, 13310.
[42] M. Quintana, M. Grzelczak, K. Spyrou, B. Kooi, S. Bals, G. Van Tendeloo, P. Rudolf, M. Prato, *Chem. Commun.* **2012**, *48*, 12159.
[43] T. Skaltsas, X. X. Ke, C. Bittencourt, N. Tagmatarchis, *J. Phys. Chem. C* **2013**, *117*, 23272.
[44] J. Zheng, H. Zhang, S. Dong, Y. Liu, C. Tai Nai, H. Suk Shin, H. Young Jeong, B. Liu, K. Ping Loh, *Nat. Commun.* **2014**, *5*.
[45] G. Eda, H. Yamaguchi, D. Voiry, T. Fujita, M. Chen, M. Chhowalla, *Nano Lett.* **2011**, *11*, 5111.
[46] Y.-H. Lee, X.-Q. Zhang, W. Zhang, M.-T. Chang, C.-T. Lin, K.-D. Chang, Y.-C. Yu, J. T.-W. Wang, C.-S. Chang, L.-J. Li, T.-W. Lin, *Adv. Mater.* **2012**, *24*, 2320.
[47] P. Delporte, F. Meunier, C. Phamhuu, P. Vennegues, M. J. Ledoux, J. Guille, *Catal. Today* **1995**, *23*, 251.
[48] K. Zhou, S. Jiang, C. Bao, L. Song, B. Wang, G. Tang, Y. Hu, Z. Gui, *RSC Adv.* **2012**, *2*, 11695.
[49] J. A. Barnard, *Trans. Faraday Soc.* **1960**, *56*, 72.
[50] A. A. Tsyganenko, F. Can, A. Travert, F. Mauge, *Appl. Catal., A* **2004**, *268*, 189.
[51] T. Weber, J. C. Muijsers, H. vanWolput, C. P. J. Verhagen, J. W. Niemantsverdriet, *J. Phys. Chem.* **1996**, *100*, 14144.
[52] C. Lee, H. Yan, L. E. Brus, T. F. Heinz, J. Hone, S. Ryu, *ACS Nano* **2010**, *4*, 2695.
[53] G. L. Frey, R. Tenne, M. J. Matthews, M. S. Dresselhaus, G. Dresselhaus, *Phys. Rev. B* **1999**, *60*, 2883.
[54] J. M. Chen, C. S. Wang, *Solid State Commun.* **1974**, *14*, 857.
[55] D. Yang, S. J. Sandoval, W. M. R. Divigalpitiya, J. C. Irwin, R. F. Frindt, *Phys. Rev. B* **1991**, *43*, 12053.
[56] A. S. Goloveshkin, I. S. Bushmarinov, N. D. Lenenko, M. I. Buzin, A. S. Golub, M. Y. Antipin, *J. Phys. Chem. C* **2013**, *117*, 8509.
[57] L. Houben, A. N. Enyashin, Y. Feldman, R. Rosentsveig, D. G. Stroppa, M. Bar-Sadan, *J. Phys. Chem. C* **2012**, *116*, 24350.
[58] H. S. S. Ramakrishna Matte, A. Gomathi, A. K. Manna, D. J. Late, R. Datta, S. K. Pati, C. N. R. Rao, *Angew. Chem. Int. Ed.* **2010**, *49*, 4059.
[59] P. Joensen, E. D. Crozier, N. Alberding, R. F. Frindt, *J. Phys. C: Solid State Phys.* **1987**, *20*, 4043.
[60] A. S. Berdinsky, L. T. Chadderton, J. B. Yoo, A. K. Gutakovsky, V. E. Fedorov, L. N. Mazalov, D. Fink, *Appl. Phys. A Mater. Sci. Process.* **2005**, *80*, 61.
[61] X. L. Li, Y. D. Li, *Chem. Eur. J.* **2003**, *9*, 2726.
[62] W. M. R. Divigalpitiya, R. F. Frindt, S. R. Morrison, *Science* **1989**, *246*, 369.
[63] A. V. Krasheninnikov, F. Banhart, *Nat. Mater.* **2007**, *6*, 723.
[64] T. Isshiki, K. Nishio, H. Saijo, M. Shiojiri, Y. Yabuuchi, N. Takahashi, *Microsc. Res. Tech.* **1993**, *25*, 325.
[65] J. Brivio, D. T. L. Alexander, A. Kis, *Nano Lett.* **2011**, *11*, 5148.
[66] R. J. Smith, P. J. King, M. Lotya, C. Wirtz, U. Khan, S. De, A. O'Neill, G. S. Duesberg, J. C. Grunlan, G. Moriarty, J. Chen, J. Z. Wang, A. I. Minett, V. Nicolosi, J. N. Coleman, *Adv. Mater.* **2011**, *23*, 3944.
[67] T. R. Thurston, J. P. Wilcoxon, *J. Phys. Chem. B* **1999**, *103*, 11.
[68] K. A. Shaffei, M. M. H. Ayoub, M. N. Ismail, A. S. Badran, *Eur. Polym. J.* **1998**, *34*, 553.
[69] S. Balendhran, J. Deng, J. Z. Ou, S. Walia, J. Scott, J. Tang, K. L. Wang, M. R. Field, S. Russo, S. Zhuiykov, M. S. Strano, N. Medhekar, S. Sriram, M. Bhaskaran, K. Kalantar-zadeh, *Adv. Mater.* **2013**, *25*, 109.
[70] R. Fivaz, E. Mooser, *Phys. Rev.* **1967**, *163*, 743.
[71] F. Kremer, A. Schonhals, *Broadband Dielectric Spectroscopy* Springer, Berlin **2003**.
[72] R. A. Sheldon, I. Arends, G. J. Ten Brink, A. Dijksman, *Acc. Chem. Res.* **2002**, *35*, 774.